Journal of Computational Physics **160,** 662–682 (2000)
doi:10.1006/jcph.2000.6481, available online at http://www.idealibrary.com on IDEAL®

A Volume of Fluid Based Method for Fluid Flows with Phase Change

Samuel W. J. Welch and John Wilson

Department of Mechanical Engineering, University of Colorado at Denver, Denver, Colorado 80217
E-mail: sam@carbon.cudenver.edu

Received August 27, 1999; revised January 27, 2000

This paper presents a numerical method directed towards the simulation of flows with mass transfer due to changes of phase. We use a volume of fluid (VOF) based interface tracking method in conjunction with a mass transfer model and a model for surface tension. The bulk fluids are viscous, conducting, and incompressible. A one-dimensional test problem is developed with the feature that a thin thermal layer propagates with the moving phase interface. This test problem isolates the ability of a method to accurately calculate the thermal layers responsible for driving the mass transfer in boiling flows. The numerical method is tested on this problem and then is used in simulations of horizontal film boiling.

Key Words: two-phase flow; boiling.

I. INTRODUCTION

Boiling flows are ubiquitous in the energy and processing industries due to the fact that phase change processes are an efficient way to transport heat. Despite decades of research there are still many aspects of boiling flows that are not well understood. The small spatial scales and fast time constants of many of the physical processes associated with boiling hinder the acquisition of experimental data. During the last two decades computational methods have been developed to provide solutions for fluid flow problems with moving interfaces separating gas and liquid phases. There is now a small but growing body of literature on the application of these methods to boiling flows. It is evident that these methods will help provide insight into many aspects of boiling flows heretofore unattainable.

The computation of boiling flows remains one of the most challenging realms of computational fluid dynamics. These flows are characterized by the discontinuity across the phase interface of many of the flow variables. These discontinuities pose several computational difficulties requiring special treatment. In addition, the location of the phase interface is not known a priori and must be found as part of the solution procedure. Early methods that

0021-9991/00 $35.00

addressed these difficulties were of the Lagrangian type in which computational elements move with the phase interface thereby enabling the special treatment of the region proximal to the phase interface. The papers of Son and Dhir [1] and of Welch [2] provide simulation results in which it is clear that Lagrangian based methods have a limited applicability due to their inability to cope with gross interfacial motion or changes in interface topology. Later methods overcame this limitation by implementing Eulerian based approaches. Juric and Tryggvason [3] used source terms in the continuity equation and the energy equation in an enhancement of the method of Unverdi and Tryggvason [4] to simulate horizontal film boiling. Son and Dhir [5] used a similar idea in a modification of the level set method of Sussman *et al.* [6] enabling them to perform simulations of axisymmetric horizontal film boiling. Their simulations of water near the critical state enabled them to provide a detailed description of the bubble release pattern during horizontal film boiling which corroborated previous experimental results.

This purpose of this paper is to introduce a modification of the volume of fluid (VOF) method suitable for the simulation of boiling flows. We feel that the VOF method has features that make it a viable option for simulations of the type discussed above. One desirable feature is that the interface is advected with a conservation equation. This results in calculations that preserve the volumes of the two phases in flows without mass transfer. We note that the level set method of Sussman *et al.* [6], used by Son and Dhir [5], does not have this volume preservation property. More recent level set implementations have addressed this problem [7] through the addition of a volume preservation constraint and can likely be extended to the mass transfer case. Another desirable feature is that the interfacial geometry associated with the VOF method may be used to construct heat flux vectors on both the liquid and the vapor side of the interface that take into account the discontinuity of the conductivity and of the temperature gradient. We note that similar calculations are possible with the level set method as well as with the method of Tryggvason. A one-dimensional similarity solution will be presented that isolates the ability of a method to accurately calculate the thermal layers responsible for driving the mass transfer in boiling flows.

We consider incompressible Newtonian fluids with behavior described in both phases by the set of partial differential equations.

$$\rho\left(\frac{\partial \mathbf{v}}{\partial t} + \mathbf{v}\cdot\nabla\mathbf{v}\right) = -\nabla P + \rho\mathbf{g} + \nabla\cdot[\mu(\nabla\mathbf{v} + (\nabla\mathbf{v})^T)] \tag{1}$$

$$\nabla\cdot\mathbf{v} = 0 \tag{2}$$

$$\rho c_p\left(\frac{\partial \vartheta}{\partial t} + \mathbf{v}\cdot\nabla\vartheta\right) = \nabla\cdot(k\nabla\vartheta) + \Phi. \tag{3}$$

Here $\mathbf{g}$ is the gravitational force and $\mathbf{v}$, P, c_p, ρ, ϑ, μ, k, and Φ are the fluid velocity, pressure, specific heat, density, temperature, viscosity, conductivity, and viscous dissipation, respectively.

II. SPECIAL TREATMENT OF THE INTERFACIAL REGIONS

Interface tracking. The presence of the two phases requires that some approach must be implemented to advect the phase interface. We advect the interface using Young's enhancement [8] of the VOF method [9]. In our code, Young's method is implemented at the end

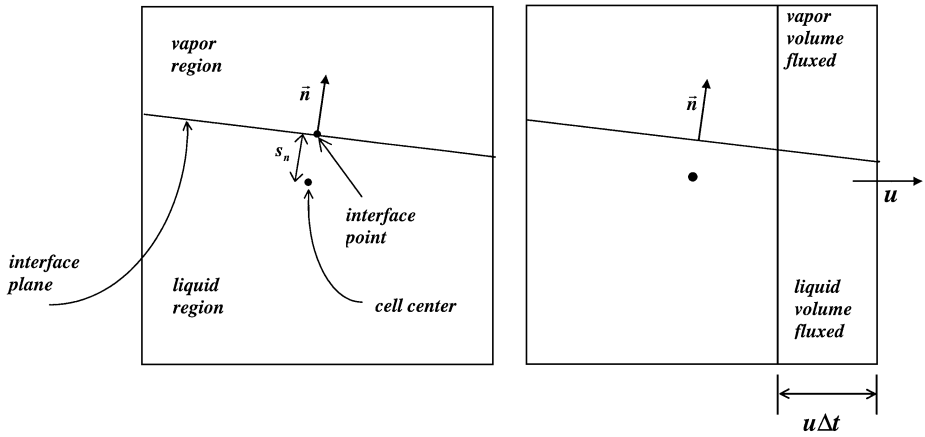

FIG. 1. Mixture cell with piecewise linear interface. Left, cell geometry; right, cell flux calculation.

of a time cycle to calculate the new density field using the conservation of mass statement for each cell

$$\frac{\partial}{\partial t}\int_{V_c}\rho\, dV + \int_{S_c}\rho\mathbf{v}\cdot\mathbf{n}\, dS = 0, \tag{4}$$

where V_c is the cell volume and S_c is the cell surface. Once the new cell densities are found, the cell void fractions are calculated

$$\alpha = \frac{\rho - \rho_g}{\rho_l - \rho_g}. \tag{5}$$

Detailed description of Young's method may be found in Refs. [10, 11]. Our implementation of Young's method may be summarized as the following sequence of steps.

(1) The phase interface is modeled as a piecewise linear curve. Figure 1 shows a typical two-phase cell with an embedded phase interface. The orientation of the curve within each two-phase cell is determined by the unit normal vector,

$$\mathbf{n} = \frac{\nabla\alpha}{|\nabla\alpha|}. \tag{6}$$

The gradients in this calculation use a nine-point stencil that is known to produce a more accurate normal vector [11].

(2) Given the orientation of the planar surface that represents the interface in a cell, determine the location of the oriented surface such that the surface partitions the cell into liquid and gas regions of the correct volume based upon the void fraction (volume fraction of liquid) of the cell. These steps are often referred to as the interface reconstruction steps [11].

(3) Given the location of the planar interface in each two-phase cell and the velocity at a junction face between two cells, the mass flux is determined from simple volumetric considerations. A typical geometric calculation of this sort is shown in Fig. 1. Once the mass is fluxed across the cell boundaries in one direction, the interface is reconstructed

before mass is fluxed in the second direction. This approach is referred to as a direction split approach [10].

Mass transfer. Mass transfer across the phase interface is modeled in a manner inspired by Juric and Tryggvason [3]. We consider a computational cell containing a volume of the liquid phase adjacent to a volume of the vapor phase. We may write a mass balance for each phase as

$$\frac{d}{dt}\int\limits_{V_g(t)} \rho\, dV + \int\limits_{S_g(t)} \rho \mathbf{v}\cdot\mathbf{n}\, dS + \int\limits_{S_I(t)} \rho(\mathbf{v}-\mathbf{v}_s)\cdot\mathbf{n}\, dS = 0 \tag{7}$$

$$\frac{d}{dt}\int\limits_{V_l(t)} \rho\, dV + \int\limits_{S_l(t)} \rho \mathbf{v}\cdot\mathbf{n}\, dS - \int\limits_{S_I(t)} \rho(\mathbf{v}-\mathbf{v}_s)\cdot\mathbf{n}\, dS = 0. \tag{8}$$

Here V_l, S_l, V_g, and S_g are the volume and surface of the liquid and vapor regions, respectively. S_I is the phase interface at the common boundary of the two regions, moving with the velocity, $\mathbf{v}_s$. On S_I the normal vector $\mathbf{n}$ points into the liquid phase. Summing these, taking into account the incompressibility of each phase, and noting that the overall volume is invariant we obtain the conservation of mass statement for the cell volume,

$$\int\limits_{S_c} \mathbf{v}\cdot\mathbf{n}\, dS + \int\limits_{S_I(t)} \|(\mathbf{v}-\mathbf{v}_s)\|\cdot\mathbf{n}\, dS = 0. \tag{9}$$

Here, $\|\Psi\|$ indicates the jump in Ψ across the phase interface and S_c is the surface bounding the computational cell. Use of the mass and energy jump conditions at the interface

$$\|\rho(\mathbf{v}-\mathbf{v}_s)\|\cdot\mathbf{n} = 0 \tag{10}$$

$$\|\rho h(\mathbf{v}-\mathbf{v}_s)\|\cdot\mathbf{n} = -\|\mathbf{q}\|\cdot\mathbf{n} \tag{11}$$

allows us to express the jump term in the conservation of mass equation as

$$\|(\mathbf{v}-\mathbf{v}_s)\|\cdot\mathbf{n} = \left(\frac{1}{\rho_l}-\frac{1}{\rho_g}\right)\frac{\|\mathbf{q}\|\cdot\mathbf{n}}{h_{lg}}. \tag{12}$$

Here h is the enthalpy and $h_{lg} = h_g - h_l$ is the latent heat of vaporization while $\mathbf{q}$ is the heat flux vector. In this work, we consider the phase interface to be at the saturation temperature of the liquid pressure

$$\vartheta_s = \vartheta_{sat}(P_l). \tag{13}$$

The set of equations, Eq. (11) through Eq. (13), incorporates various simplifying assumptions. Surface properties other than surface tension are neglected. We neglect kinetic energy and viscous work terms as well as surface tension work terms in the energy jump and we neglect the viscous dissipation in the energy equation. These are common approximations in the analysis of liquid-vapor phase change phenomena [18] and have been used in the numerical studies of liquid-vapor phase change [1, 2, 5]. The temperature condition given by Eq. (13) is a common approximation for which justification may be found in [5]. We

note that there are various conditions other that Eq. (13) appearing in the literature (see, for example, Refs. [2, 3]) but the exact condition is still an open question of physics. At any rate, these simplifying assumptions leave us with a model that contains the dominant physics. The inclusion of terms resulting from the relaxation of these assumptions, should they be deemed important, is straightforward.

The energy jump condition indicates the dependence of the mass transfer rate across the interface on the heat flux vector in the normal direction in both the liquid and vapor phases. The heat flux vector will generally be discontinuous and any smoothing of this vector will distort the mass transfer amount. We utilize the interface geometry associated with the VOF method to construct a proper heat flux jump source term for use in Eq. (12). By a proper heat flux jump, we mean that the normal components of the temperature gradients are calculated without reaching across the phase interface. The required geometry is provided in the advection step described above and is shown in Fig. 1. Given the unit normal vector, **n**, and the parameter s_n which provides the location of the interface we apply the temperature condition, Eq. (13), to the point located at the center of the piecewise linear segment (the interface point in Fig. 1). It is then a simple matter to calculate liquid side temperature gradients as well as vapor side temperature gradients. We then are able to construct a proper heat flux jump across the phase interface by multiplying the normal temperature gradients in each phase by their corresponding conductivities. In addition, it is important that the cells proximal to the interface but not containing the phase interface see proper temperature gradients in the convection and diffusion terms of the energy equations. We ensure this by using the temperature gradients used in forming the energy jump condition to extrapolate liquid and vapor temperatures at mixture cell centers thus ensuring that the cells neighboring mixture cells also see the proper temperature gradients.

Surface tension model. The momentum equations are augmented using the continuum surface tension model of Brackbill *et al.* [12]

$$\rho(\alpha)\left(\frac{\partial \mathbf{v}}{\partial t} + \mathbf{v}\cdot\nabla\mathbf{v}\right) = -\nabla P + \rho(\alpha)\mathbf{g} + \nabla\cdot[\mu(\alpha)(\nabla\mathbf{v} + (\nabla\mathbf{v})^T)] + \sigma\kappa\nabla\tilde{\alpha}, \quad (14)$$

where $\tilde{\alpha}$ is a smoothed void field and κ is the curvature of the surface defined by this smoothed void field. Due to the smoothing, the surface tension force is applied to a transition region a few cells thick centered at the interface. The curvature calculation is implemented using second-order central differences and discussion on the effects of smoothing and on accuracy maybe found in [12]. The density and viscosity vary with the void field as

$$\rho(\alpha) = \rho_l\alpha + \rho_g(1-\alpha) \quad (15)$$

$$\mu(\alpha) = \mu_l\alpha + \mu_g(1-\alpha). \quad (16)$$

The surface tension is constant in this formulation thus the method is not appropriate for flows in microgravitational environments in which the temperature dependence of the surface tension provides the driving impetus for fluid motion.

Summarizing these developments, for computational cells containing the phase interface we use the augmented momentum equation, Eq. (14), the modified conservation of mass statement, Eq. (9), and energy jump condition Eq. (11). The discontinuity of the velocity field, the velocity gradients, and the viscosity in this formulation are treated by smoothing

which is a departure from the philosophy used in treating the discontinuous temperature gradients and conductivity. The method presented in this paper is directed towards flows driven by mass transfer due to phase change which motivates the special treatment of the interfacial heat flux vector described above. Future efforts will address better the coupling of the discontinuities associated with the momentum equation to the discontinuities associated with the energy equation.

III. NUMERICAL APPROXIMATIONS

The spatial discretization of the governing partial differential equations is obtained using a traditional MAC staggered grid [13] with scalars located at cell centers and velocity components located at cell edges. All spatial derivatives are centered with the exception of the convection terms in the momentum and the energy equations. Due to the discountinuity in velocity across the phase interface, the momentum convection terms are discretized using a second order ENO method [14]. The convection terms in energy are discretized using the Leonard method [15]. Note that a high-resolution scheme is not necessary for the energy equation, as we are not discretizing energy convection terms across the phase interface.

The temporal discretization may best be described as a semi-implicit forward Euler method. We begin a time cycle by solving the explicit energy equation in the bulk phases,

$$\vartheta^{n+1} = \vartheta^n + \delta t \left\{ -\mathbf{v} \cdot \nabla \vartheta + \frac{\kappa}{\rho c_p} \nabla^2 \vartheta \right\}^n. \tag{17}$$

The new temperature field is then used to form the interfacial heat flux jump appearing in the mass source term and the continuity and momentum equations are discretized in time as

$$\int_{S_c} \mathbf{v}^{n+1} \cdot \mathbf{n}\, dS + \int_{S_I(t)} \left(\frac{1}{\rho_l} - \frac{1}{\rho_g} \right) \frac{\|\mathbf{q}^{n+1}\| \cdot \mathbf{n}}{h_{lg}}\, dS = 0 \tag{18}$$

$$\mathbf{v}^{n+1} = \mathbf{v}^n - \delta t (\mathbf{v} \cdot \nabla \mathbf{v})^n - \frac{\delta t}{\rho^n} \{ \nabla P^{n+1} + (\rho \mathbf{g})^n + \nabla \cdot [\mu (\nabla \mathbf{v} + (\nabla \mathbf{v})^T)]^n + \sigma (\kappa \nabla \tilde{\alpha})^n \}. \tag{19}$$

The new time velocity is eliminated from these discrete equations and the resulting pressure equation is solved by an interative method. The simulations in this paper use the ILU preconditioned conjugate gradient squared (CGS) method of Sonneveld [16]. Once the new time pressure is obtained the new time velocity is found from the discrete momentum equations and the new density field is found from the discretization of Eq. (4)

$$\rho^{n+1} = \rho^n + \delta t \int_{S_c} \rho \mathbf{v}^{n+1} \cdot \mathbf{n}\, dS. \tag{20}$$

As discussed earlier, Young's method is employed at this stage of the calculation. We note that cells that are not mixture cells or are not adjacent to mixture cells do not require this

calculation. Once the new density field is found, the new void fraction may be calculated along with the mixture cell interfacial geometry.

The scheme we have just described is second order in space and first order in time. The scheme has time step restrictions due to the explicit treatment of the convection and diffusion terms in the momentum and energy equations. The scheme also has a time step restriction due to the explicit treatment of the surface tension terms. This limit is usually expressed as restricting a capillary wave in an infinite medium to travel no more than half a cell width during a time step. This limit is generally the most restrictive of the three and satisfaction of this limit often results in solutions that are converged in time, even with a first-order method.

IV. ONE-DIMENSIONAL VERIFICATION PROBLEMS WITH MASS TRANSFER

The Stefan problem. We consider first the one-dimensional Stefan problem considered by Son and Dhir [5] and shown in Fig. 2. The liquid and vapor are considered incompressible and are initially in quiescent equilibrium. The vapor experiences an increase in temperature on the solid boundary and a thermal profile develops in the vapor driving mass transfer at the interface. In this flow, the vapor will be motionless while the liquid is pushed away from the solid boundary with the interface also moving away from the solid boundary. The liquid profiles are uniform and the energy equation in the vapor phase may be expressed as

$$\frac{\partial \vartheta}{\partial t} = \alpha \frac{\partial^2 \vartheta}{\partial x^2}, \qquad 0 \le x \le \delta(t), \tag{21}$$

where $\delta(t)$ is the coordinate of the phase interface. The problem is closed with the boundary conditions

$$\begin{aligned} \vartheta(x = \delta(t), t) &= \vartheta_{sat} \\ \vartheta(x = 0, t) &= \vartheta_{wall} \end{aligned} \tag{22}$$

and the interfacial energy jump condition

$$\rho_g v_s h_{lg} = -k \left. \frac{\partial \vartheta}{\partial x} \right|_{x=\delta(t)}. \tag{23}$$

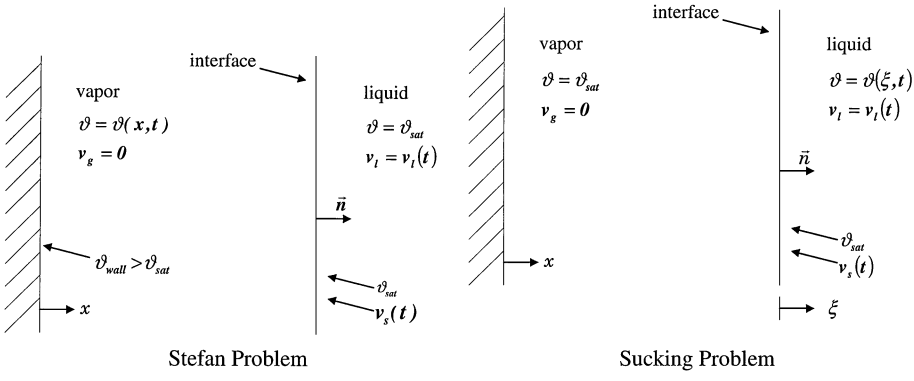

FIG. 2. Left, domain definition for Stefan problem; right, domain definition for sucking interface problem.

The Neumann solution to this one-phase Stefan problem may be shown to apply to the flow considered here and is given by [17]

$$\delta(t) = 2\lambda\sqrt{\alpha t} \tag{24}$$

$$\vartheta(x,t) = \vartheta_{wall} + \left(\frac{\vartheta_{sat} - \vartheta_{wall}}{\mathrm{erf}(\lambda)}\right)\mathrm{erf}\left(\frac{x}{2\sqrt{\alpha t}}\right), \tag{25}$$

where $\mathrm{erf}(x)$ is the error function and λ is a solution to the transcendental equation.

$$\lambda \exp(\lambda^2)\mathrm{erf}(\lambda) = \frac{c_p(\vartheta_{wall} - \vartheta_{sat})}{h_{lg}\sqrt{\pi}}. \tag{26}$$

We simulate this case using the properties of water at the three saturation pressures 101.3, 571.0, and 14044.0 kPa. These saturation pressures correspond to the density ratios $\rho_l/\rho_g =$ 1605.2, 301.4, and 7.08, respectively. We use a grid spacing of $\Delta x = 0.1$ mm and set only the first computational cell to be vapor with the second cell being a two-phase cell. The temperature profiles are initialized as a simple linear profile with the wall temperature set to 25 K higher than the saturation temperature.

Figure 3 shows the liquid velocity as well as the interface position as functions of time for both the analytic solution and the simulation at each pressure. The simulation results are in excellent agreement with the analytic solution despite the fact that so few vapor cells are used to describe the early time temperature profiles. This result is due the fact that the analytic temperature solution is actually close to a linear function. In addition, this

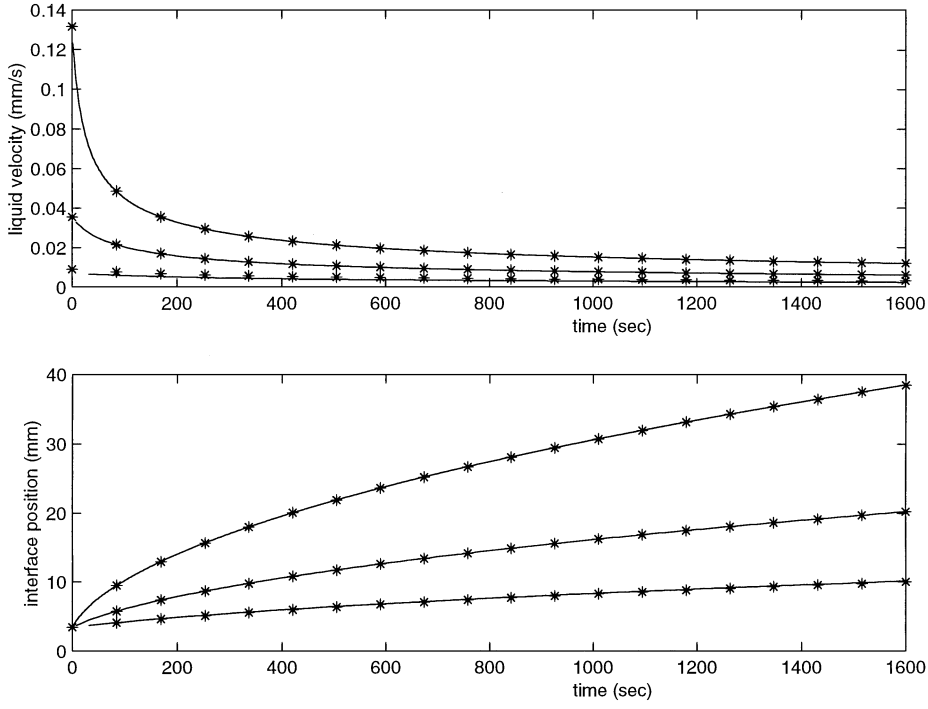

FIG. 3. Liquid velocity and interface position for Stefan problem. Top curve, Psat = 101.3 kPa; middle curve, Psat = 571.0 kPa; bottom curve, Psat = 14044.0 kPa.

analytic solution is characterized by an extensive thermal layer on the vapor side of the interface. Such a thermal layer poses little difficulty numerically in that the temperature gradient driving the mass transfer is easily resolved without requiring fine grid resolution. The situation for boiling flows in which the mass transfer is driven by temperature gradients associated with thin thermal layers will be more computationally challenging. With this in mind we present a one-dimensional test case in which a thin thermal layer on the liquid side drives the mass transfer.

The sucking interface problem. We consider a one-dimensional flow in which the liquid and vapor phases are incompressible. The problem configuration is shown in Fig. 2 and we note that the vapor phase is motionless, existing at the saturation temperature while the liquid phase will move at a uniform velocity and exist in a metastable state at a distance removed from the phase interface. This situation will result in a thin thermal layer moving with the interface. The diffusive spreading of the thermal layer will be counteracted somewhat by a sucking of the thermal layer towards the interface thus the thermal layer will tend to remain thin.

We make the following transformation of the spatial coordinate

$$\xi = x - \int_0^t v_s(t)\,dt. \tag{27}$$

This transformation defines the coordinate ξ such that the interface is located at $\xi = 0$. The energy equation in the liquid phase transforms to

$$\frac{\partial \vartheta}{\partial t} + (v - v_s)\frac{\partial \vartheta}{\partial \xi} = \alpha \frac{\partial^2 \vartheta}{\partial \xi^2} \tag{28}$$

with boundary and initial conditions

$$\begin{aligned} \vartheta(\xi = 0, t) &= \vartheta_{sat} \\ \vartheta(\xi \to \infty, t) &= \vartheta_o \\ \vartheta(\xi, t = 0) &= \vartheta_o, \end{aligned} \tag{29}$$

where ϑ_o is the liquid temperature in the bulk phase and ϑ_{sat} is the saturation temperature. At the interface we have the energy and mass jump conditions

$$\rho(v_l - v_s)h_{lg} = -k\frac{\partial \vartheta}{\partial \xi}\bigg|_{\xi=0} \tag{30}$$

$$-\rho_g v_s = \rho(v_s - v_l). \tag{31}$$

Defining the constants

$$B = \frac{\alpha}{C\beta}, \qquad \beta = \frac{\rho_g}{\rho_l}, \qquad C = \frac{k}{\rho_g h_{lg}} \tag{32}$$

and using the mass jump condition to eliminate the liquid velocity we arrive at a simplified energy equation for the liquid side

$$\frac{\partial \vartheta}{\partial t} - \beta v_s \frac{\partial \vartheta}{\partial \xi} = \alpha \frac{\partial^2 \vartheta}{\partial \xi^2}, \tag{33}$$

where the interface velocity is given by

$$v_s = C \left. \frac{\partial \vartheta}{\partial \xi} \right|_{\xi=0}. \tag{34}$$

We obtain a similarity solution to the energy equation by introducing the parameter

$$\eta = \sqrt{\frac{1}{2\alpha}} \frac{\xi}{\sqrt{t}} \tag{35}$$

and implementing the transformation

$$\vartheta(x,t) = B\phi(\eta). \tag{36}$$

This leads to the ordinary differential equation defining our similarity solution

$$\phi'' + (\eta + \phi'(0))\phi' = 0 \tag{37}$$

with transformed boundary conditions

$$\begin{aligned} B\phi(\eta = 0) &= \vartheta_{sat} \\ B\phi(\eta \to \infty) &= \vartheta_o. \end{aligned} \tag{38}$$

This non-linear ordinary differential equation must be solved numerically and in the results that follow care was taken to ensure that a converged solution was used for comparison purposes. Once obtained, $\phi(\eta)$ provides the thermal profile as well as the interface and liquid velocities for arbitrary fluid properties and arbitrary times.

We simulate this problem with our method using the properties of water at the saturation pressure of 1 atm. We start our simulations by initializing the liquid temperature profile to the temperature profile of the similarity solution at 0.1 s. The grid spacing used in the simulations employs three successively refined grids. The coarse resolution grid has a mesh spacing of $\Delta x = 0.2$ mm. The medium and fine resolution grids have mesh spacing of $\Delta x = 0.1$ mm and $\Delta x = 0.05$ mm, respectively. The initial thermal layer thickness is 0.476 mm thus the successive grids capture the initial thermal layer with approximately three cells, five cells, and ten cells, respectively. Figure 4 shows the resulting liquid speed and interface positions with respect to time for the three grid resolutions. Figure 5 shows the temperature profile at the terminal time (1.1 s) of the simulation.

The simulation results indicate that the fine grid solution has converged and that the temperature profile, the interface position, and the liquid speed are accurately calculated. In particular we note that the curvature of the temperature profile as well as the discontinuous temperature gradient are accurately calculated. The three differing resolution grids may be used to obtain estimates for the order of the method using the computed interface position, liquid velocity, and temperature gradient at the interface. The resulting estimates for the order of the method are 1.42, 2.05, and 2.12, respectively. This test problem provides an indication of the ability of the method to follow a thin thermal layer moving with the interface thus accurately calculating the temperature gradients responsible for the mass transfer across the interface.

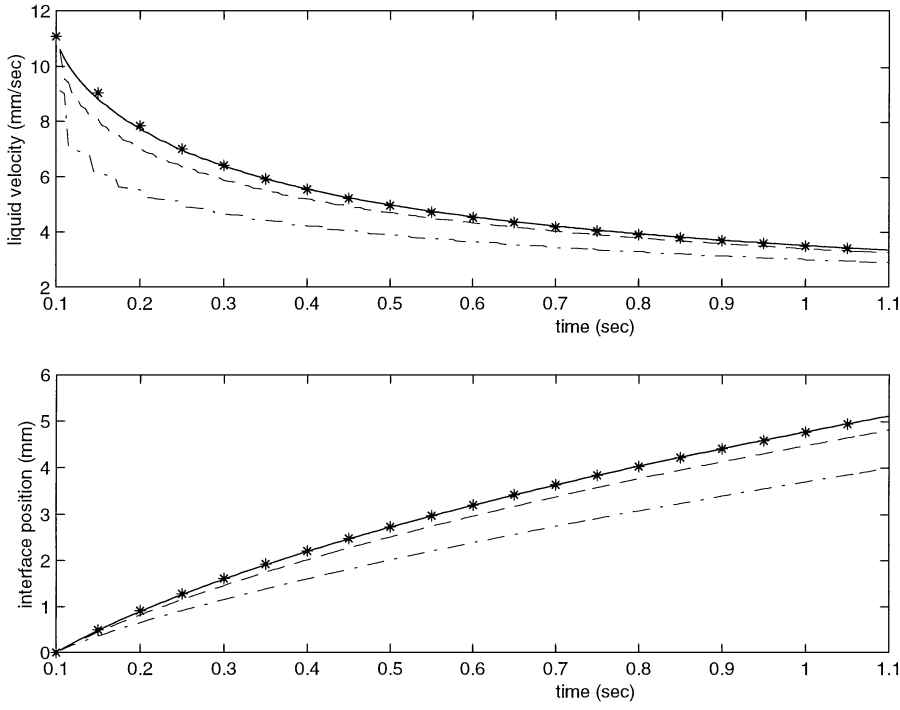

FIG. 4. Liquid velocity and interface position for sucking interface problem at Psat = 101.3 kPa. – – –, coarse grid; – – –, medium grid; ——, fine grid; ∗, similarity solution.

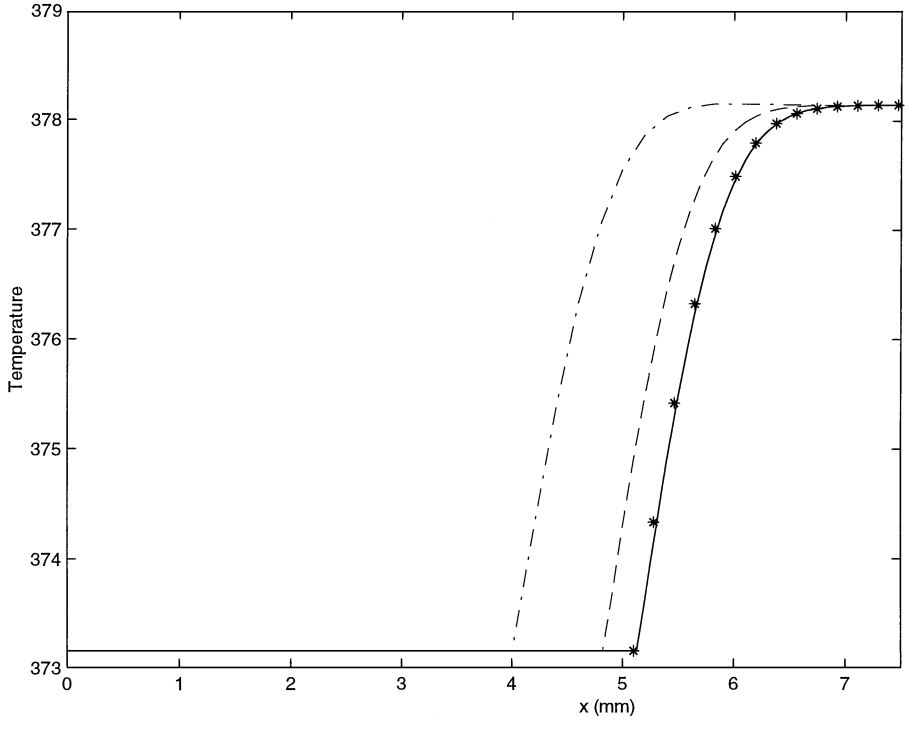

FIG. 5. Temperature profile for sucking interface problem at Psat = 101.3 kPa and 1.1 s. – – –, coarse grid; – – –, medium grid; ——, fine grid; ∗, similarity solution.

V. SIMULATION OF HORIZONTAL FILM BOILING

The regimes associated with boiling liquids situated above heated walls are usually described in terms of a "boiling curve" [18]. Briefly, for low wall superheat (wall temperature above the saturation temperature at the system pressure), the liquid does not vaporize and the regime is termed the convective heat transfer regime. As the wall superheat is increased, nucleation sites start to appear and individual bubbles start to form and leave the wall due to bouyancy forces. This region is known as the nucleate boiling regime. As the wall superheat is increased the bubbles begin to coalesce on the surface and we enter a regime in which large portions of the heated surface are covered with vapor. This region is known as fully developed nucleate boiling and for high enough wall superheat, transition boiling (transition refers to transition from fully developed nucleate boiling to film boiling). Finally for high enough wall superheat, the entire surface is immersed in vapor and we have entered a regime known as film boiling. Film boiling is particularly amenable to numerical simulation as the difficulties associated with modeling a contact line (the curve defined by the intersection of the phase interface and the solid wall) do not exist. There exists a handful of correlations for the case of a horizontal film boiling and these correlations generally assume some sort of vapor bubble release mechanism for the vapor as it leaves the film and is removed due to the buoyant forces. One such correlation due to Berenson [19] assumes that the vapor bubbles are spaced in a square pattern separated by a distance equivalent to the most dangerous Taylor wavelength given by

$$\lambda_o = 2\pi \left(\frac{3\sigma}{(\rho_l - \rho_g) g_y} \right)^{1/2}. \tag{39}$$

His correlation also assumes a uniform film thickness and a bubble diameter and height that are proportional to the bubble spacing. Conservation of mass and momentum in the vapor film as well as the assumption that heat is transferred across the film due to conduction only enabled him to arrive at an expression for the Nusselt number

$$Nu = 0.425 \left(\frac{\rho_g (\rho_l - \rho_g) g_y h_{lg}}{k_g \mu_g [\vartheta_{wall} - \vartheta_{sat}]} \right)^{1/4} (\lambda_o)^{3/4}. \tag{40}$$

This correlation and the physical situation modeled by it are inherently three-dimensional. We will present two-dimensional simulations with the understanding that the numerical results cannot completely capture the physics of three-dimensional film boiling but these simulations do present useful test problems with which to develop methods directed towards simulating flows with mass transfer. We note also that there are correlations in the literature thought to be more accurate than the Berenson correlation [18]. We do not expect that two-dimensional simulations can predict Nusselt numbers with the fidelity necessary to require comparison to the more accurate correlations.

We consider a two-phase fluid with surface tension $\sigma = 0.1$ N/m, latent heat $h_{lg} = 10.0$ kJ/kg, saturation pressure $P_{sat} = 1.0135 \times 10^5$ Pa, and saturation temperature $\vartheta_{sat} = 500$ K. The liquid properties used are $k_l = 40.0$ W/m · K, $\mu_l = 0.1$ Pa · s, $\rho_l = 200.0$ kg/m^3, $C_{pl} = 400.0$ J/kg · K, and the vapor properties used are $k_g = 1.0$ W/m · K, $\mu_g = 0.005$ Pa · s, $C_{pg} = 200.0$ J/kg · K, $\rho_g = 5.0$ kg/m^3. The high mechanical and thermal diffusivities are used as the corresponding low cell Reynolds and Peclet numbers allow for the demonstration of the convergence of the method on a relatively coarse sequence of computational grids. We take advantage of the symmetry in the problem and use a computational domain

with width $\lambda_o/2$ and heights of either $3\lambda_o/2$ or $3\lambda_o$. We consider the left and right vertical boundaries to be symmetry boundaries. The bottom boundary is considered a no-slip solid wall and the top boundary is open with the pressure specified. We initialize the liquid to be at the saturation state and the vapor temperature to increase linearly from the interface to the solid wall. In the results that follow we present results reflected across the left-hand symmetry boundary.

We first present results of a convergence study to ensure that our grid resolution is adequate. We consider three grids of resolution 16×48, 32×96, and 64×192. The solid wall is kept at a constant temperature of 10 K above the saturation temperature. The fine grid simulations initalizes the fifth row of cells with the half cosine wave void profile $\alpha = 0.5 + 0.4 \cos(2\pi x/\lambda_o)$. The coarse and medium resolution grids initialize the void field such the interface is located at an identical spatial location. Figure 6 shows the phase interface calculated on the three grids as the first bubble is about to leave the film. Figure 6

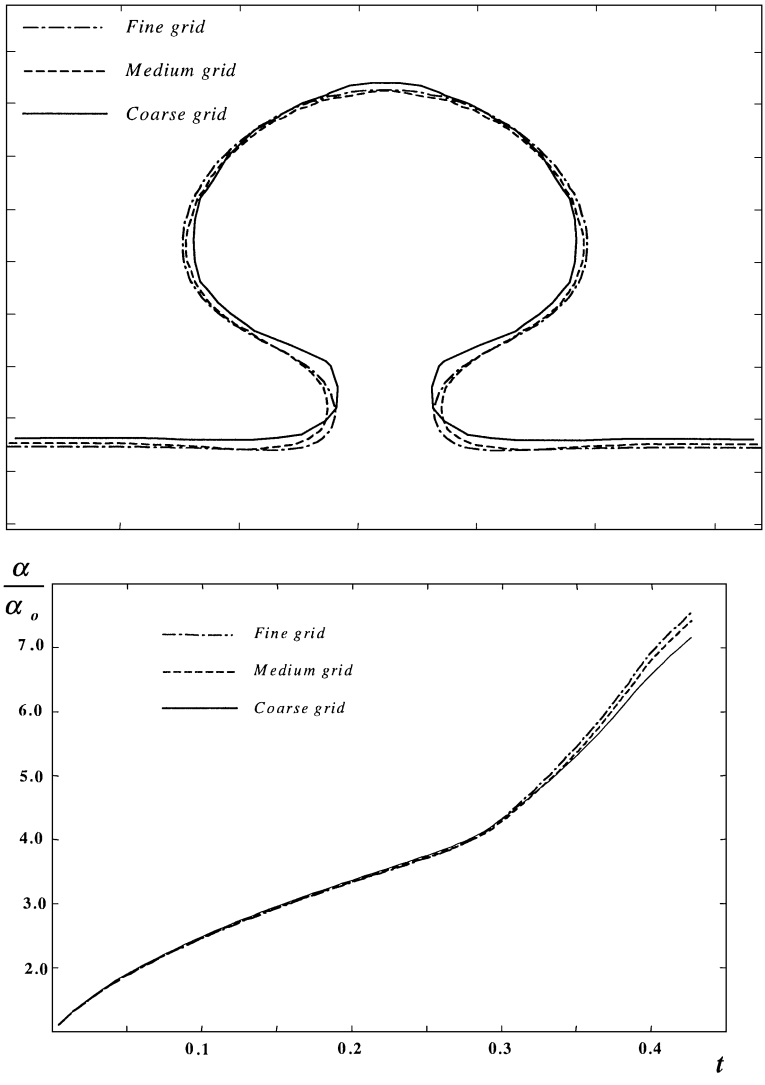

FIG. 6. Bubble shape and ratio of vapor void to initial vapor void for three different grid resolutions.

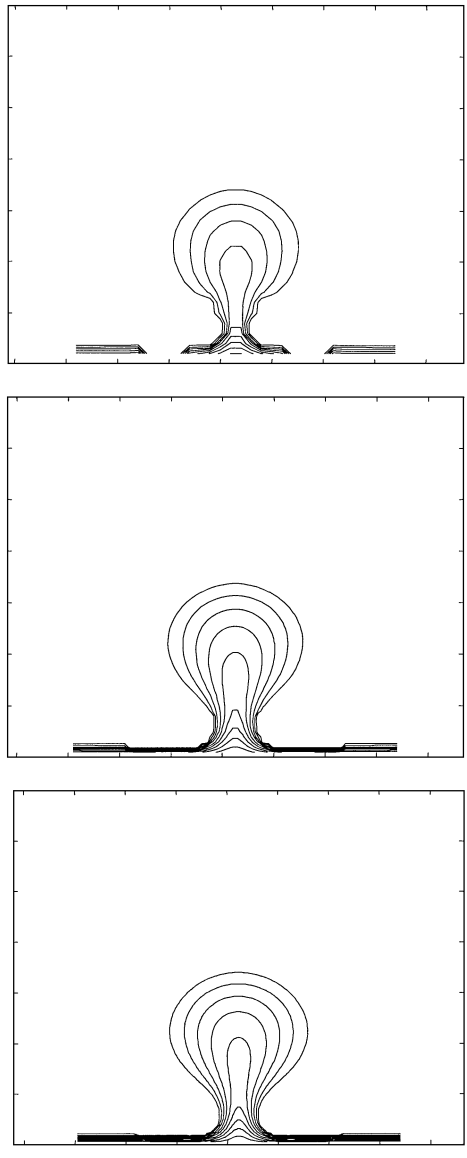

FIG. 7. Temperature contours spaced 1 K apart for three different grid resolutions. Top, coarse grid; middle, medium grid; bottom, fine grid.

also shows the vapor volume relative to the initial vapor volume. Figures 7 and 8 give temperature contours and contours of both components of velocity, respectively. From these figures we conclude that the medium resolution grid adequately represents the case under consideration. These simulations were run at a time step equal to one-fourth the capillary limit of the finest resolution grid. Later simulations using the medium resolution grid were run at a time step approximately three times as large with no discernable difference. This corroborates our earlier statement that observing the capillary limit often results in solutions converged in time.

Film boiling is a quasi-steady phenomenon and we expect that the transients caused by the artificial prescription of initial conditions will eventually die off leaving us with a numerical

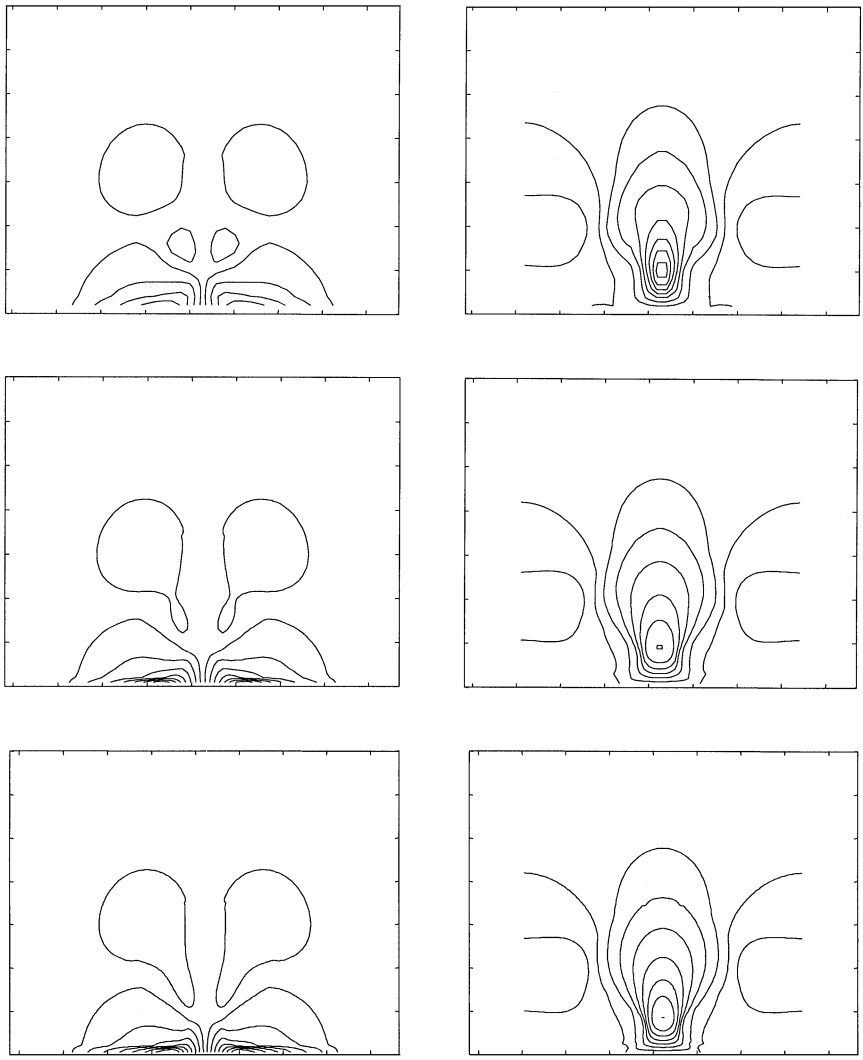

FIG. 8. Velocity contours for three different grid resolutions. Left column, x-direction component, 10 contours spaced evenly from −1.36 to 1.36 m/s; right column, y-direction component, 10 contours spaced evenly from −1.01 to 1.01m/s. Top, coarse grid; middle, medium grid; bottom, fine grid.

solution exhibiting quasi-steady periodicity. In our simulations the early transients are typified by the release of a few larger bubbles before the quasi-steady bubble release pattern is realized. Shown in Figs. 9 and 10 are simulation results exhibiting this quasi-steady behavior for wall superheat values of 5 degrees Celsius and 10 degrees Celsius, respectively. The local Nusselt number is calculated as the dimensionless heat flux through the wall

$$Nu = \frac{\lambda_o}{(\vartheta_{wall} - \vartheta_{sat})} \frac{\partial \vartheta}{\partial y}\bigg|_{y=0}. \tag{41}$$

The Nusselt number in the figures is an averaged value over the width of the solid wall. The maximum and minimum Nusselt numbers correspond to minimum and maximum average film thickness, respectively. The interface plots in Figs. 9 and 10 depict the interface at times near to the minimums and maximums of the averaged Nusselt number. We note that the small bubbles appearing in Figs. 9 and 10 are not properly resolved on the medium

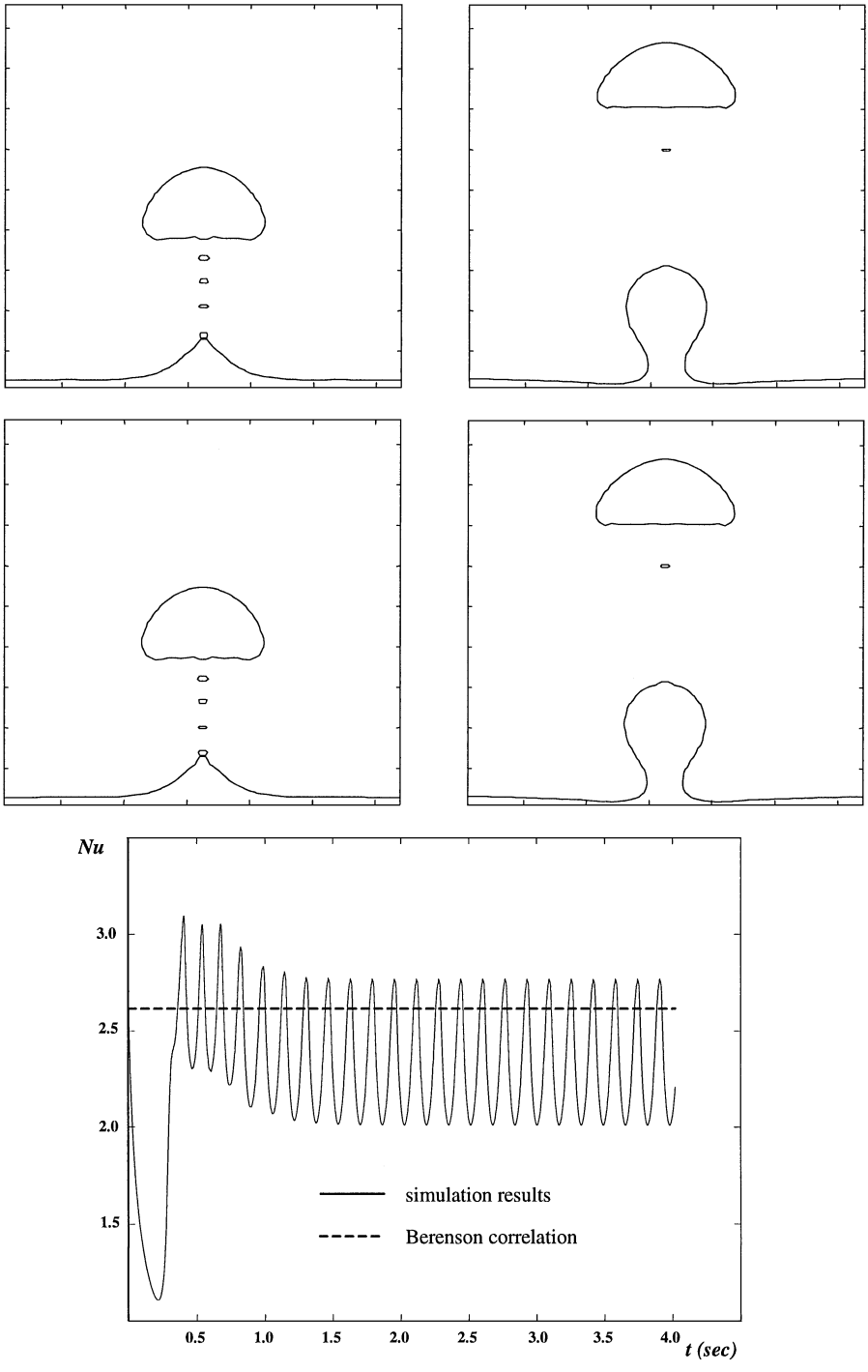

FIG. 9. Simulation results for $\Delta\vartheta = 5$ K.

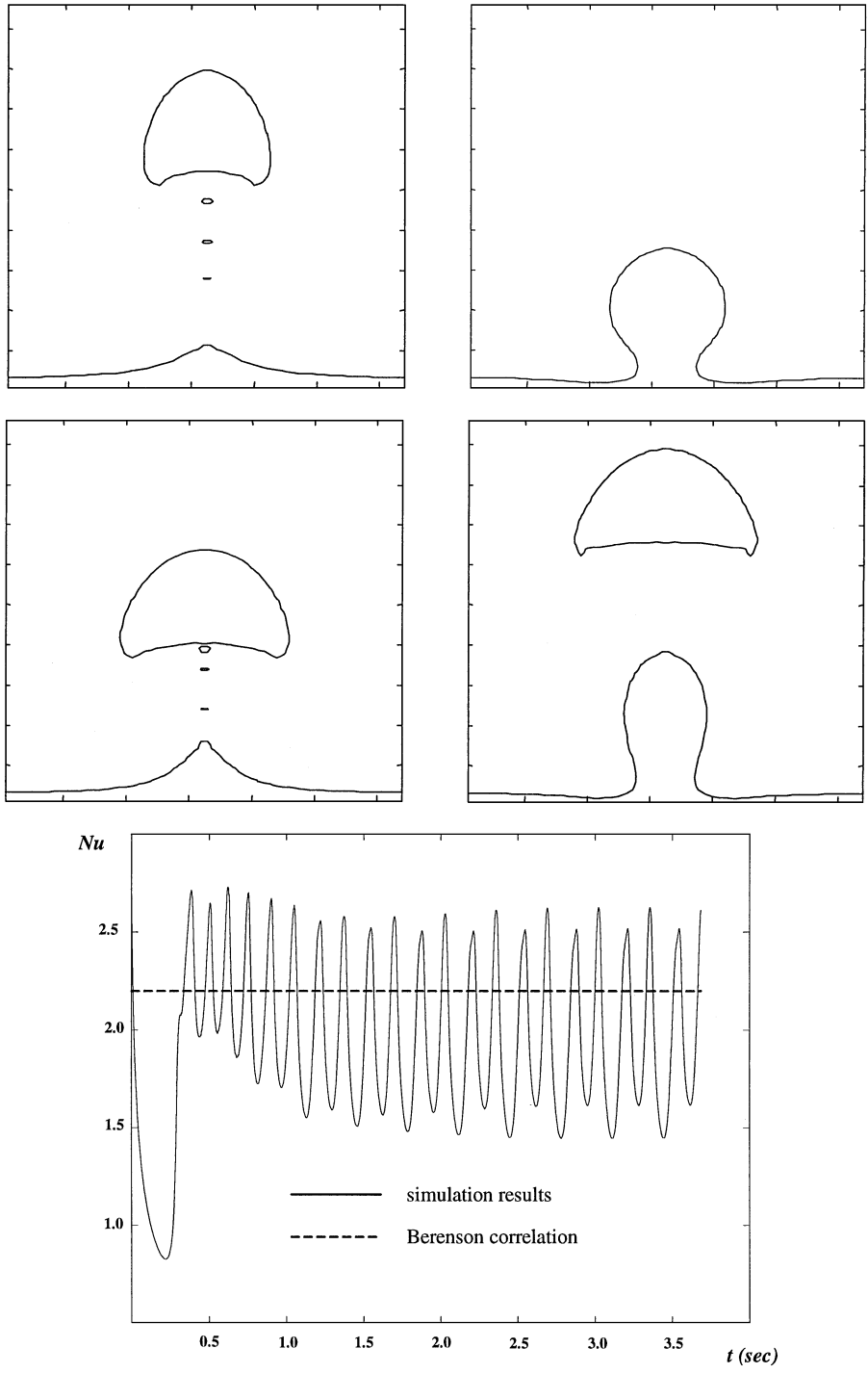

FIG. 10. Simulation results for $\Delta\vartheta = 10$ K.

resolution grid but their appearance on the fine resolution grid is similar. This indicates that they are not likely the flotsam and jetsam commonly appearing with VOF methods on too coarse a grid.

At a wall superheat of 5 K we observe that as the bubble is near departure, the film is depleted of vapor and hence the Nusselt number is at the peak value. Similarly, in the period prior to the bubble formation the vapor film grows hence the Nusselt number is at the minimum value. At a wall superheat of 10 K we make similar observations but note that the quasi-steady Nusselt number has two distinct minimums and two distinct maximums. The figure indicates that there two distinct patterns of bubble release defined by the distance that the previously released bubble has moved. Figure 11 shows clearly the single release

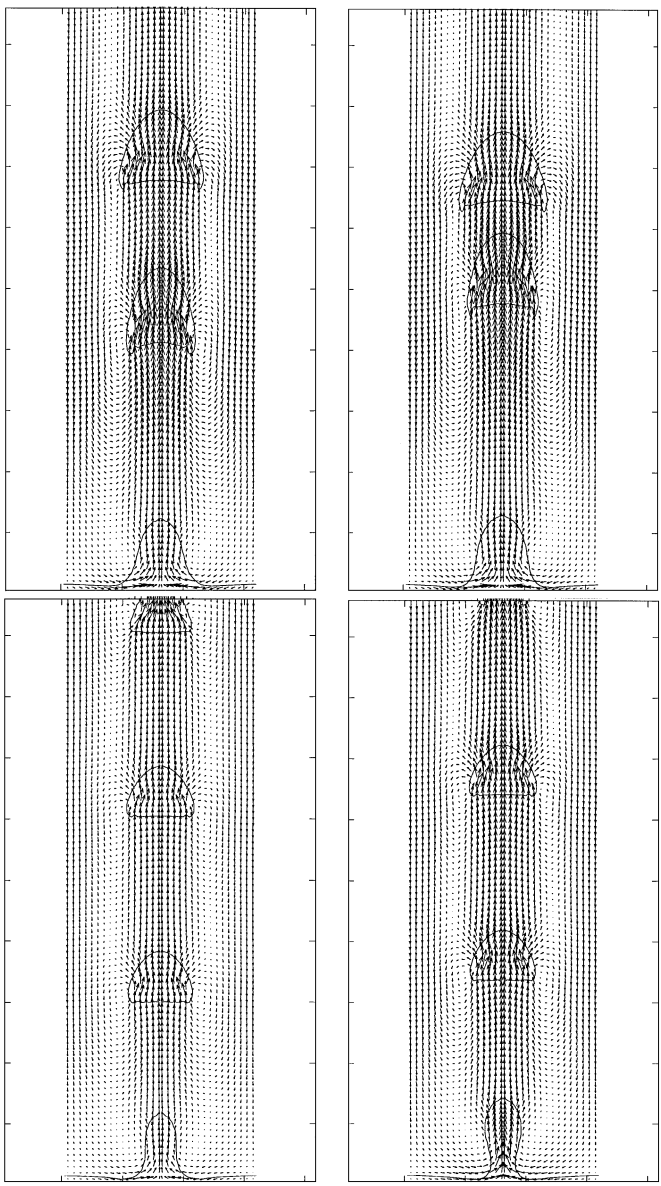

FIG. 11. Bubble release patterns and velocity fields at time step 35,000 (left) and at time step 40,000 (right). Top, $\Delta\vartheta = 10$ K; bottom, $\Delta\vartheta = 5$ K.

pattern for the low-wall superheat case and the two bubble release patterns for the high-wall superheat case. Figure 11 was generated by running the simulations on a grid twice the height as that used in the previous plots. We note that in both cases the quasi-steady behavior was identical as that exhibited in the previous simulations indicating that the behavior described is not affected by the location of the outflow boundary.

These simulations exhibit expected quasi-steady behavior in that a steady pattern of bubble release is reached in which ellipsoidal bubbles exit the vapor film and are transported away due to buoyant forces. Juric and Tryggvason [3] obtained early transient results that exhibit remarkably different behavior with regard to the bubble release mechanism. In one of their simulations they obtained mushroom shaped bubbles that remained connected to the film by a vapor jet. We obtain similar results by considering a fluid with properties that give the following dimensionless parameters,

$$\frac{\rho_l}{\rho_g} = 5.18, \qquad \frac{\mu_l}{\mu_g} = 3.46, \qquad \frac{k_l}{k_g} = 2.37, \qquad \frac{C_{pl}}{C_{pg}} = 0.864, \qquad Pr = \frac{\mu_l C_{pl}}{k_l} = 1.92.$$

Following [3], we define scales for length, velocity, temperature, and heat flux,

$$l_o = \left(\mu_l^2/g\rho_l^2\right)^{1/3}, \qquad (l_o g)^{1/2}, \qquad \rho_g h_{lg}/\rho_l C_{pl}, \qquad \rho_g h_{lg} k_l/\rho_l C_{pl} l_o.$$

The Morton number and a capillary parameter (Mo, Ca) have the values

$$Mo = \frac{\mu_l^4 g}{\sigma^3 \rho_l} = 1.0 \times 10^{-6}, \qquad Ca = \frac{\vartheta_{sat} C_{pl} \sigma}{\rho_g h_{lg}^2 l_o} = 0.020.$$

Except for the Mo, these parameters correspond to para-Hydrogen at 8.0 atm [20] and are similar to the parameters used in [3]. We simulate this case using a 64×320 grid with the same boundary conditions as were used in the previous simulations with the exception that the dimensionless wall heat flux, $q_w = 20.0$, is specified rather than the wall temperature. The interface is initialized in the fifth row of computational cells by setting the void fraction for cells in this row to $\alpha = 0.5 + 0.4\cos(2\pi x/\lambda_o)$. This corresponds to the non-dimensional interface height $y = 7.8 + 0.58\cos(2\pi x/\lambda_o)$.

Figure 12 shows the resulting interface plots as well as temperature contours and velocity vector plots for three time cycles during the simulation. The time cycles are chosen to be spaced a similar distance apart as the time cycle at which plots are given in the similar simulation of Juric and Tryggvason [3]. These results show a mushroom shape developing followed by a jet that supplies hot vapor to the developing bubble. The vapor jet persists and the bubble does not pinch off as in the previous simulations. The bubble shapes, the velocity field, and the temperature field are all quite similar to the results obtained in [3]. The one notable difference is that the skirts found on the large bubbles in [3] have fragmented and formed a smaller bubble in the present simulation. This difference may be due to the fact that as interfacial features such as the skirt width approach the size of the grid spacing the VOF method tends to fragment continuous interfaces whereas the method of Tryggvason does not. We do not compare the Nusselt number as our initial conditions are quite different in terms of the film thickness and shape which are important factors affecting the Nusselt number.

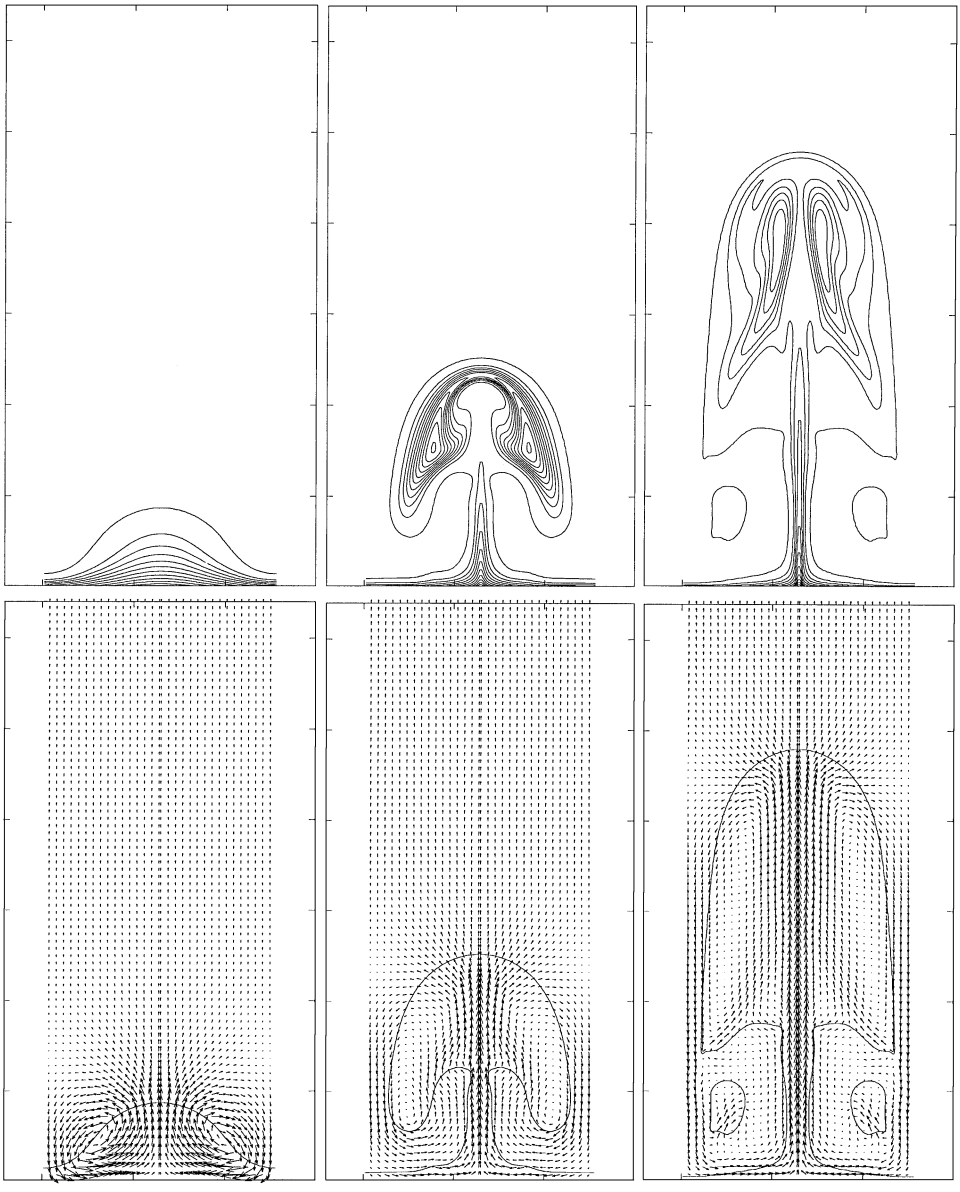

FIG. 12. Simulation results exhibiting mushroom shaped bubbles. Left column, $t = 22.7$; center column, $t = 42.2$; right column, $t = 61.7$.

VI. CONCLUSIONS

An approach to computing boiling flows based on Young's enhancement of the VOF method has been presented. The interface geometry associated with Young's method provides a convenient basis with which to accurately calculate the discontinuous normal component of the heat flux vector that drives the mass transfer. A similarity solution has been presented that provides a rigorous test of a computational method's ability to accurately compute the temperature profile in boiling flows. We feel that Young's enhancement of VOF is a viable alternative to simulating gas-liquid flows including the case with mass transfer.

We note extension of Young's method to three dimensions is straightforward and the mass transfer model described in this paper generalizes easily to three dimensions.

REFERENCES

1. G. Son and V. K. Dhir, *ASME J. Heat Transfer* **119**, 535 (1997).
2. S. W. J. Welch, *Int. J. Heat Mass Transfer* **41**(12), 1655 (1998).
3. D. Juric and G. Tryggvason, *Int. J. Multiphase Flow* **24**(3), 387 (1998).
4. S. O. Unverdi and G. C. Tryggvason, *J. Comput. Phys.* **100**, 25 (1992).
5. G. Son and V. K. Dhir, *ASME J. Heat Transfer* **120**, 183 (1998).
6. M. Sussman, P. Smereka, and S. J. Osher, *J. Comput. Phys.* **100**, 25 (1992).
7. M. Sussman, E. Fatemi, P. E. Smereka, and S. J. Osher, *Comput. & Fluids* **27**(5–6), 663 (1998).
8. D. L. Youngs, Time-dependent multi-material flow with large fluid distortion, in *Numerical Methods for Fluid Dynamics*, edited by K. W. Morton and M. J. Baines (Academic Press, New York, 1982), p. 27.
9. C. W. Hirt and B. D. Nichols, *J. Comput. Phys.* **39**, 201 (1981).
10. M. Rudman, *Int. J. Numer. Methods Fluids* **24**, 671 (1997).
11. W. J. Rider and D. B. Kothe, *J. Comput. Phys.* **141**, 112 (1998).
12. J. U. Brackbill, D. B. Kothe, and C. Zemach, *J. Comput. Phys.* **100**, 335 (1992).
13. F. E. Harlow and J. E. Welch, *Phys. Fluids* **8**, 2182 (1965).
14. T. C. Chang, T. Y. Hou, B. Merriman, and S. J. Osher, *J. Comput. Phys.* **124**, 449 (1996).
15. B. P. Leonard, *Phys. Fluids* **8**, 2182 (1965).
16. P. Sonneveld, *SIAM J. Sci. Statist. Comput.* **10**(1), 36 (1984).
17. V. Alexiades and A. D. Solomon, *Mathematical Modeling of Melting and Freezing Processes* (Hemisphere, Washington, DC/New York, 1993).
18. P. Van Carey, *Liquid-Vapor Phase Change Phenomena* (Taylor & Francis, London, 1992).
19. P. J. Berenson, *J. Heat Transfer* **83c**(3), 351 (1961).
20. R. D. McCarty, J. Hord, and H. M. Roder, *Selected Properties of Hydrogen*, NBS Monograph 168, 1981.